Langmuir

Article

pubs.acs.org/Langmuir

Quantum Dot Thermometry Evaluation of Geometry Dependent Heating Efficiency in Gold Nanoparticles

Laura M. Maestro,[†] Patricia Haro-González,[†] Ana Sánchez-Iglesias,[‡] Luis M. Liz-Marzán,[‡,§] José García Solé,[†] and Daniel Jaque*[,†]

[†]Fluorescence Imaging Group, Departamento de Física de Materiales, Instituto Nicolás Cabrera, Facultad de Ciencias, Universidad Autónoma de Madrid, 28049 Spain.

[‡]Bionanoplasmonics Laboratory, CIC biomaGUNE, Paseo de Miramón 182, 20009 Donostia − San Sebastián, Spain

[§]Ikerbasque, Basque Foundation for Science, 48011 Bilbao, Spain

ABSTRACT: Quantum dot based thermometry, in combination with double beam confocal microscopy, was used to investigate the absorption/heating efficiency of gold nanoparticles with different morphologies (nanorods, nanocages, nanoshells, and nanostars), all of them with an intense localized surface plasmon resonance within the first biological window, at around 808 nm. The heating efficiency was found to be strongly dependent on the geometry of the nanostructure, with the largest values found for gold nanorods and long-edge gold nanostars, both of them with heating efficiencies close to 100%. Gold nanorods and nanocages were found to have the largest absorption cross section per unit mass among all the studied geometries, emerging as optimum photothermal agents with minimum metal loading for biosystems.

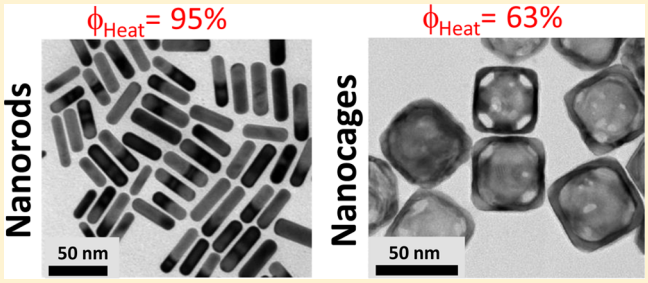

INTRODUCTION

Hyperthermia is defined as a process by which body temperature increases above the standard value (37 °C). In some cases, this temperature increment is exploited to drive malignant cells and tissues (constituting, for example, a cancer tumor) up to the cytotoxic level, that is, 43−48 °C. At these temperatures, "soft" effects such as protein denaturation take place in such a way that "nonaggressive" cell death is induced and/or the cell resistance against traditional treatments (such as chemotherapy or radiotherapy) is temporally reduced.[1] In other cases, local temperature is increased even further (>50 °C), leading to the so-called "thermal ablation", which corresponds to severe damage and cell death through coagulative necrosis and membrane lysis.[2] Hyperthermia treatments have also been used to increase drug delivery efficiency by reducing vasoconstrictions (i.e., increasing bloodstream) as well as by favoring intracellular drug incorporation thanks to the temperature-induced increase of cell membrane permeability.[3] Several types of nanoparticles (NPs) have been proposed to achieve selective, accurate, and efficient hyperthermia treatments.[4−6] These NPs can be classified into three main groups, depending on their particular role in the thermal treatment: (i) Nanoparticles acting as nanothermometers, that is, devoted to provide real-time thermal sensing over the treated cells and tissues.[7,8] These NPs, such as quantum dots, fluorescent nanogels, rare earth doped complexes, or rare earth doped nanocrystals,[9−14] are required to avoid excessive heating that would create undesirable damage in healthy cells and tissues surrounding malignant ones, as it has been done in several previous works, some of them taking advantage of the possible combination of such nanoparticles with other nanoparticles providing heating capabilities (nanoheaters).[15−19] There are, indeed, review articles describing the state of the art in nanothermometry.[8,20,21] (ii) Nanoparticles for temperature activated drug delivery[22,23] (such as mesoporous silica nanoparticles or metallic nanoparticles) and finally, (iii) nanoparticles for selective local heating (nanoheaters, hearafter NHts).[24] The reduced size of NHts allows for efficient intracellular incorporation and for long distance transport through the bloodstream, so that they can be incorporated into cancer cells and tissues. Once incorporated, NHts induce a local temperature increase when externally stimulated so that they can be used for remote heating of cancer cells and tissues.[25]

The fast progress of nanoparticle synthesis procedures has contributed to the development of a wide variety of biocompatible NHts. These can be classified, depending on the external stimulus used to activate heating, into two families: magnetic nanoheaters (M-NHts) and photoactivated NHts (PA-NHts). In the case of M-NHts, heating is induced by the application of an external oscillating magnetic field, due to different physical mechanisms including direct motion of M-NHts and/or hysteresis induced magnetic energy storage.[26,27] M-NHts have been, indeed, used in clinical and preclinical

Received: September 5, 2013
Revised: January 14, 2014

   dx.doi.org/10.1021/la403435v | *Langmuir* XXXX, XXX, XXX−XXX

studies resulting in successful treatment of different types of tumors.[28,29] On the other hand, PA-NHts are capable of releasing heat when excited by optical radiation. In this case, hyperthermia treatments are based on the selective incorporation of PA-NHts into cancer tissues/cells, followed by optical excitation leading to localized temperature increase.[30] Photothermal therapies based on the use of PA-NHts do not require complicated or expensive experimental facilities but offer great flexibility. Nevertheless, their practical application is severely limited by the reduced penetration length of light into human tissues. It is nowadays widely accepted that significant optical penetration into a human body would require the use of certain spectral ranges, where light absorption by water and other components of biological specimens is minimum.[31,32] In particular, light radiation of wavelength around 808 nm seems to be particularly adequate for highly selective photothermal treatments.[33] The simultaneous negligible water absorption and reduced scattering cross section of tissues at 808 nm allow for long penetration depths into tissues making possible real in-depth photothermal treatments.[34] On the other hand, light sources based on fiber coupled diodes operating at around 808 nm provide stable, high brightness and excellent spectral and optical quality beams, at moderate manufacturing costs.

Among the various nanoparticles capable of efficient light-induced heating, gold nanoparticles (hereafter GNPs) are undoubtedly the most popular ones.[35] Moreover GNPs, have attracted great attention in the past due to their multifunctional character. They were initially introduced in biophotonics as high brightness multiphoton excited fluorescent biolabels.[36,37] Interestingly, GNPs are receiving renewed interest due to their ability as photothermal agents.[38,39] Both fluorescence and heating properties of GNPs are based on localized surface plasmon resonances (SPR), which correspond to collective oscillations of conduction electrons in the NPs. A SPR is induced when the GNPs are illuminated by an electromagnetic field at a certain wavelength, the so-called surface plasmon resonance wavelength (λ_{SPR}). When a GNP is illuminated at λ_{SPR}, heat is generated because of the relaxation of surface currents (process along which energy is delivered to the surrounding medium). The spectral location of λ_{SPR} depends on the particle dimensions as well as on particle shape,[40] since in the collective surface charge motion a resonance between a light induced electromagnetic force acting on surface electrons and their restoring/damping force takes place, and this resonance condition depends on GNP geometry and size. This is, indeed, an outstanding advantage of GNPs since predesigned λ_{SPR} can be achieved through adequate tailoring of GNP morphology. Indeed, it is possible to find in the literature a variety of GNPs with λ_{SPR} matching the "optimum" tissue transparency value of 808 nm, including the following:

(i) Gold Nanoshells (GNSs). They comprise a dielectric (silica) core surrounded by a thin gold shell. By an appropriate choice of the core diameter to shell thickness ratio, GNSs can be optically engineered so that their λ_{SPR} can be controllably tuned within the visible-NIR range. GNSs have been successfully used for infrared thermal ablation of human breast cancer cells,[41] for example.

(ii) Gold Nanorods (GNRs). These are solid quasi-cylindrical nanoparticles with typical widths of 10−20 nm and lengths ranging from few tens to over one hundred nanometers, so that their aspect ratios (length/diameter) typically range between 2 and 10.[42] The spectral location of their surface plasmon resonance wavelength depends not only on their width and length but also on the precise geometry of their edges. The exact dependence of λ_{SPR} on the particular GNR geometry is far from being simple but this multiparameter dependence constitutes a flexible route to obtain GNRs with λ_{SPR} at around 808 nm. GNRs have been successfully used in the past for both "in vivo" and "in vitro" photothermal therapy of tumors and cancer cells with low (well below W/cm^2) laser intensities.[43,44]

(iii) Gold Nanocages (GNCs). They consist of hollow six-sided gold dices. In this case, the SPR can be spectrally tuned by varying either the wall thickness or the edge length. GNCs have been demonstrated to be promising materials for biomedical applications including "in vivo" multiphoton excited fluorescence imaging and simultaneous photothermal treatments.[45]

(iv) Gold Nanostars (GNSts). These are solid gold nanospheres from which different lobes protrude. These lobes can be "short", so we get short-edge GNSts (GNSts-s), or "long", so we get long-edge GNStars (GNSt-l). The position of their corresponding λ_{SPR} depends on a variety of parameters, including the number of lobes per GNSt and the dimensions of both the spherical core and the lobes. Based on this multiparameter dependence, the spectral position of the SPR can be tailored within a wide spectral range, covering both visible and NIR spectral ranges. GNSts have also been demonstrated to be efficient photothermal agents, with the potential addition of efficient drug delivery due to their intrinsically large surface to volume ratios.[46]

These geometries can be considered as the most popular ones, but the continuous development of novel synthesis routes is leading to a continuous appearance into scene of other GNPs with their SPR also located close to 808 nm. Nevertheless these geometries can be considered as combinations or derivations of the four basic geometries listed above. This is, for example, the case of the recently introduced gold nanohexapods.[47]

The efficiency of photothermal treatments based on any of the above-described GNPs would be given by the density of GNPs incorporated in the biosystem, the excitation laser intensity and the heating efficiency of GNPs (the fraction of the laser power reaching the GNP that is converted into heat).[47] Due to the very low fluorescence efficiency of GNPs, almost all the absorbed optical power is converted into heat.[48−50] Therefore, the heating efficiency of GNPs is given by the relative contribution of absorption cross section (σ_{abs}) to the net extinction cross section (σ_{ext}), i.e. this efficiency is a measure of absorption and scattering relative contributions ($\sigma_{ext} = \sigma_{abs} + \sigma_{scat}$), being σ_{scat} the scattering cross section. Consequently, we here consider that the heating efficiency is given by the absorption efficiency of GNPs, Φ_{abs}, defined as the fraction of the total extinction cross section related to the absorption processes, $\Phi_{abs} = \sigma_{abs}/\sigma_{ext}$. Theoretical modeling indicated that this magnitude is strongly dependent on the particular size and shape of the GNPs.[51] Indeed, previous theoretical work pointed out that both GNRs with aspect ratios close to 3 and sharp GNSts are expected to have absorption efficiencies close to unity.[51−53] On the other hand, it has been postulated that "short" GNSts as well as GNSs could show absorption efficiencies below 0.5.[54] The exact knowledge over Φ_{abs} would also allow for the experimental determination of both scattering and absorption cross sections of GNPs from the extinction cross section, a magnitude that can be determined in a straightforward manner from simple optical transmission

dx.doi.org/10.1021/la403435v | Langmuir XXXX, XXX, XXX−XXX

experiments. Indeed, the absorption and scattering cross sections of a GNP are related to the extinction cross section and absorption efficiency by two simple relations: $\sigma_{abs} = \sigma_{ext}\Phi_{abs}$ and $\sigma_{scat} = \sigma_{ext}(1 - \Phi_{abs})$. Therefore, if both extinction cross section and absorption efficiency are known, the absorption and scattering cross sections can be obtained with no need of either complex simulations or complicated experimental procedures, such as integrating photoacoustic spectroscopy. Nevertheless, despite its interest from applied and fundamental points of view, few examples can be found in the literature dealing with the influence that morphology has on the absorption efficiency of infrared excited GNPs. Some of them[51] face the problem based on purely numerical simulations. Others, such as the recently published work by Wang et al.,[47] report an estimate of the absorption efficiency of specific geometries (nanohexapods, nanorods, and nanocages) as determined by photoacoustic imaging, a technique that requires calibration with a reference sample of known heating efficiency (indocyanine green, in this case).[47,55]

In this work, we have systematically investigated the absorption efficiency of GNPs of five different geometries that lead to SPR at around 808 nm. Absorption efficiency has been experimentally determined by using quantum dot based double-beam fluorescence thermometry, which is a self-consistent technique that does not require the use of any reference system. Experimental results are discussed and compared with previously reported theoretical predictions. The obtained results allow us to identify the geometries that could optimize future GNPs photothermal treatments.

MATERIALS AND METHODS

Particle synthesis, Morphological and Optical Extinction Characterization. Figure 1 displays representative transmission electron microscopy (TEM) images of the GNPs investigated in this work (GNRs, GNSs, GNSts and GNCs). Commercially available GNRs, provided by Gold Nanorods LLC, were 8 ± 1 nm thick and 29 ± 5 nm long (Figure 1a). The GNSs investigated in this work were supplied by Nanocomposix Inc. and comprised 120 ± 5 nm diameter silica cores surrounded by 10 ± 1 nm thick gold shells (Figure 1b). GNSts and GNCs were synthesized following previously reported procedures,[56,57] which are briefly described next.

Gold Nanostars. For completeness, we investigated the absorption efficiency of both "short" and "long" GNSts (GNSt-s and GNSt-l, respectively), as defined in the Introduction, involving two different synthesis routes. As previously reported,[56] for the synthesis of GNSt-l, the seed solution was first prepared by adding a sodium citrate solution (1% wt, 5 mL) to a boiling $HAuCl_4$ solution (0.5 mM, 100 mL) under vigorous stirring. Boiling was continued for 15 min, and then the colloid was cooled down and kept at 4 °C for long-term storage. For GNSt-l synthesis, citrate-stabilized seed solution ([Au] = 0.5 mM, 13 ± 0.2 nm, 0.75 mL) was added to a mixture containing $HAuCl_4$ (0.25 mM, 50 mL) and HCl (1 M, 0.05 mL) at room temperature under moderate stirring (700 rpm). Silver nitrate (10 mM, 0.15 mL) and ascorbic acid (100 mM, 0.25 mL) were added quickly, both at the same time. The solution was stirred for 30 s during which the color rapidly turned from light-red to blue. Then, CTAB solution (15 mM, 50 mL) was added to ensure colloidal stability of the nanoparticles. The solution was centrifuged once (4000 rpm, 15 min) and redispersed in water. The resulting GNSt-l are shown in the TEM images of Figure 1c and d, and were finally constituted by central 38 ± 4 nm diameter cores, each surrounded by 17 (on average) elongated lobes (9 ± 3 thick, 46 ± 6 nm long). For the synthesis of GNSt-s, a different route was adopted, according to previous works.[57] In this case, an aqueous solution of $HAuCl_4$ (50 mM, 0.08 mL) was mixed with a polyvinylpyrrolidone (PVP) MW = 10 000 (10 mM, 15 mL) solution in *N*,*N*-dimethylformamide (DMF), followed by rapid addition of a preformed dispersion of PVP-coated Au seeds in ethanol ([Au] = 4.2 mM, 13 ± 0.2 nm, 0.04 mL), under stirring. Within 15 min, the color of the solution changed from pink to colorless and finally turned blue, indicating the formation of gold nanostars in solution. The solution was centrifuged three times (5000 rpm, 20 min) and finally dispersed in water. The resulting GNSt-s are shown in Figure 1e, f and comprised 36 ± 4 nm diameter central cores surrounded by a smaller number (10, on average) of low aspect ratio lobes (6 ± 3 nm thick, 13 ± 3 nm long).

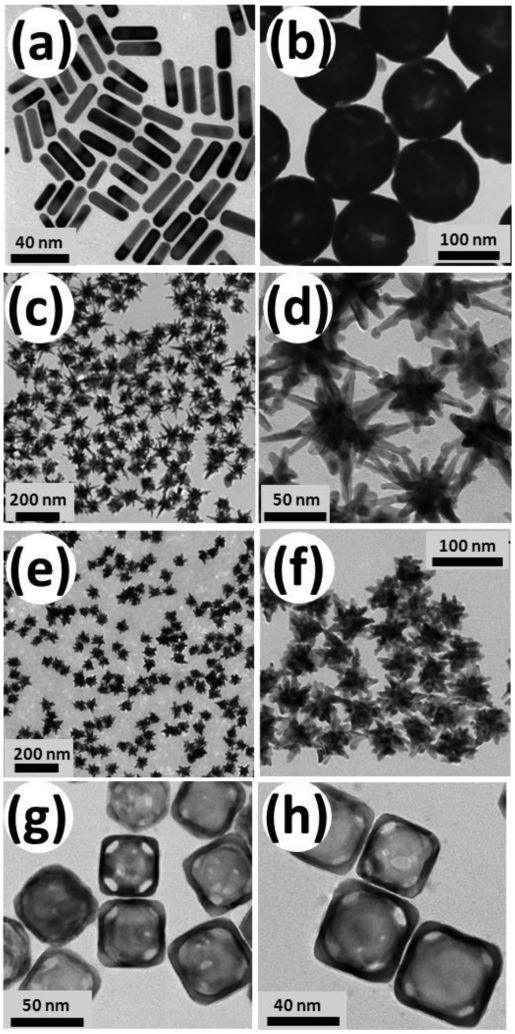

Figure 1. TEM images of the five different gold nanoparticles investigated in this work: gold nanorods (a), nanoshells (b), "long" gold nanostars (c,d), "short" gold nanostars (e,f), and gold nanocages (g,h).

Gold Nanocages. GNCs were synthesized by polyol synthesis, followed by Galvanic replacement.[58,59] In a first stage, ethyleneglycol (EG) (5 mL) was pored into a 25-mL round-bottom flask and heated under magnetic stirring in an oil bath preset to 150 °C. Then, NaHS solution in EG (3 mM, 0.06 mL) was quickly injected into the heated solution at 150 °C. Two minutes later, HCl solution in EG (3 mM, 0.5 mL) was injected into the heated reaction solution, followed by addition of PVP MW=55000 in EG (0.36 mM, 1.25 mL). After other 2 min, silver trifluoroacetate in EG (282 mM, 0.4 mL) was added to the mixture. After 30 min the reaction solution was quenched by placing the reaction flask in an ice−water bath. Then we proceeded with the Galvanic replacement reaction. An aliquot of the as-obtained silver nanocubes dispersion (1 mL) was added to 25 mL of water and refluxed for 10 min, followed by the dropwise addition of an aqueous solution of $HAuCl_4$ (1 mM, 5 mL). The mixture was then refluxed for 20 min to ensure galvanic replacement. Vigorous magnetic stirring was

dx.doi.org/10.1021/la403435v | *Langmuir* XXXX, XXX, XXX−XXX

Table 1. Characteristic Dimensions of the Five Different GNPs under Investigation in This Work[a]

geometry	dimensions	[Au], g/NP	[GNPs], NPs/cm^3	α_{ext}(808 nm), cm^{-1}	σ_{ext}(808 nm), cm^2	Φ_{abs}	σ_{abs}(808 nm), cm^2	σ_{scat}(808 nm), cm^2	σ_{abs}(808 nm)/[Au] cm^2/gr
GNRs	8 ± 1 nm width 29 ± 5 nm length	2.8×10^{-17}	1.3×10^{11}	5.9	4.5×10^{-11}	0.95 ± 0.04	4.3×10^{-11}	2.0×10^{-12}	1.5×10^{6}
GNSt-l	38 ± 4 nm core 9 ± 3 × 46 ± 6 nm lobes	1×10^{-15}	9×10^{10}	4	4.4×10^{-11}	1.02 ± 0.03	4.4×10^{-11}	0	4.4×10^{4}
GNSt-s	36 ± 4 nm core 6 ± 3 × 13 ± 3 nm lobes	5.4×10^{-16}	1.3×10^{11}	2	1.5×10^{-11}	0.43 ± 0.05	6.4×10^{-12}	8.4×10^{-12}	1.2×10^{4}
GNCs	47 ± 3 nm edge 4 ± 1 wall thickness	4.7×10^{-16}	8×10^{9}	4	5×10^{-10}	0.63 ± 0.02	3.1×10^{-10}	1.9×10^{-10}	7×10^{5}
GNSs	120 ± 5 nm Si-core 10 ± 1 nm shell	1×10^{-14}	1.3×10^{10}	2	1.5×10^{-10}	0.68 ± 0.03	1×10^{-10}	5.0×10^{-11}	1×10^{4}

[a]The GNP concentrations and the extinction coefficients at 808 nm of the five aqueous solutions of GNPs of Figure 2 are also listed. The calculated extinction cross section and the experimentally obtained absorption efficiencies are included in the last two columns.

maintained during the entire process. The solution was then centrifuged twice at 10 000 rpm for 15 min and finally redispersed in water. The resulting GNCs had a cubic morphology, with 47 ± 3 nm average edge length, framing six 4 ± 1 nm thick gold faces (Figure 1g,h).

All five types of GNPs investigated in this work were dispersed in Milli-Q water. The concentration of all GNPs ([GNP]), together with their extinction coefficients at 808 nm (α_{ext}(808 nm)) are listed in Table 1, which also includes the extinction cross sections, calculated for each case by dividing the extinction coefficient by the GNP concentration (σ_{ext}(808 nm) = α_{ext}(808 nm)/[GNP]). As a reminder, the extinction coefficient (α_{ext}) is the sum of the absorption and the scattering coefficients (α_{abs} and α_{sct}, respectively), that is, $\alpha_{ext} = \alpha_{abs} + \alpha_{scat}$.

All the solutions showed excellent colloidal stability for several months. The normalized extinction spectra of the five solutions are shown in Figure 2, as obtained with a Perkin Elmer double beam

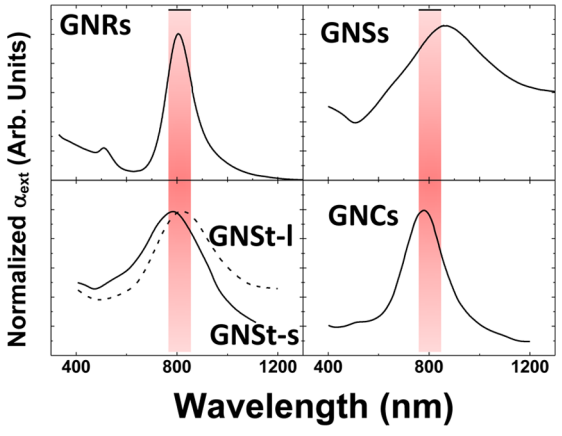

Figure 2. Normalized extinction spectra of the aqueous colloidal solutions of gold nanorods (GNRs), nanoshells (GNSs), long and short nanostars (GNSt-l and GNSt-s), and nanocages (GNCs).

spectrometer working in transmission mode (LAMBDA 1050 UV/vis/NIR spectrophotometer). All five solutions displayed extinction coefficient peaks, λ_{SPR}, close to 808 nm. The extinction spectra of the colloidal solutions were systematically monitored during experiments without observing any remarkable changes neither in the spectral position of the SPR nor in the value of the extinction coefficient. This ensures that no reshaping effects were taking place as a result of laser illumination.

Thermal Loading Measurements and Determination of Absorption Efficiency. Double beam fluorescence thermometry (DBFT) was used for the determination of Φ_{abs}. DBFT has been proven to be an adequate and reliable technique for determining the absorption efficiency of heating nanoparticles (including GNRs and carbon nanotubes) without the requirement of reference systems for calibration.[33,52] The working principle of DBFT is schematically described in Figure 3. Briefly, the solution containing the heating NPs

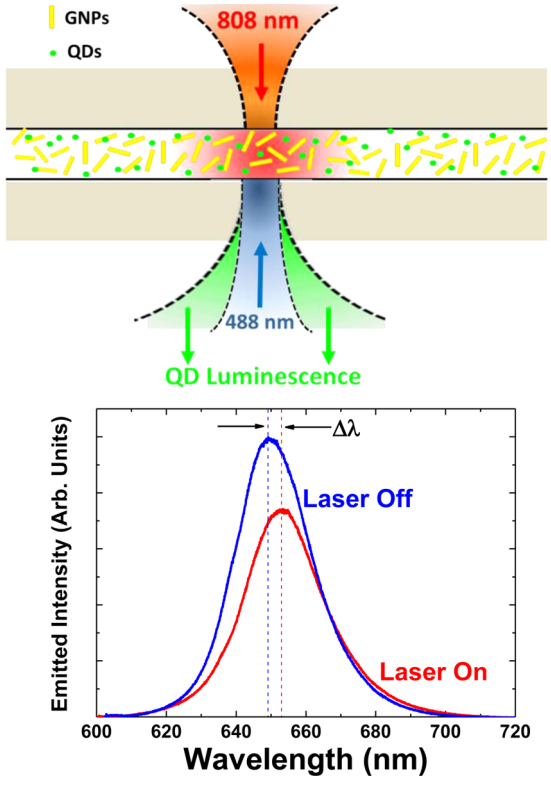

Figure 3. (Top) Schematic representation of the working principle of the double beam fluorescence thermometry (DBFT) technique used for the determination of the absorption efficiency of GNP nanoheaters. (Bottom) Characteristic emission spectra corresponding to CdSe-QDs dispersed together with GNPs in the presence/absence of the 808 nm heating laser beam (on/off conditions). The spectral shift reveals a remarkable increase in the on-focus temperature due to laser induced plasmonic heating.

is introduced in a microchamber, upon addition of a small amount of CdSe thermosensitive fluorescent quantum dots, for the purpose of thermal sensing. The resulting concentration of QDs was set to be as low as 10^9 QDs/cm^3, so that their effect on the optical absorption of the mixed solution is negligible (the extinction coefficient of the mixed solution corresponds to that of the GNPs). As described elsewhere, CdSe-QDs are well-established thermal probes for nanothermometry, on the basis of a linear shift of their photoluminescence band with

dx.doi.org/10.1021/la403435v | Langmuir XXXX, XXX, XXX−XXX

temperature.[20,60,61] For the CdSe-QDs used in this work (Invitrogen Inc., ref Q21521MP), the temperature induced spectral shift is known to be 0.1 nm/°C.[61] The mixed solution was placed within a 100 μm high and 5 mm wide μ-channel (provided by Ibidi Inc.). For DBFT, two overlapping laser beams are focused into the μ-channel with two different purposes. A first (pump) 808 nm laser beam (from a single mode diode laser) was used to excite the GNPs and so to produce a local increase of the solution's temperature. This 808 nm laser was focused into the solution by using a 50× long working distance infrared objective with a numerical aperture of 0.55. The 808 nm beam waist inside the solution was estimated from simple Gaussian optics to be $w_l \approx 0.88$ μm. Then, the magnitude of this temperature increase at focus was measured by analyzing the thermosensitive luminescence of the CdSe-QDs, which were optically excited by focusing a (probe) 488 nm laser beam in the solution. This beam, 2 mW power, was focused by using a 10× microscope objective with 0.2 numerical aperture, which leads to a beam waist of 1.4 μm. For the QD concentration and 488 nm laser power (intensity) used in this work, we verified that no thermal loading of the mixed solution due to light absorption by QDs was produced, so that light induced heating can be unequivocally related to the GNPs. The photoluminescence of CdSe-QDs was collected by the same optics used for 488 nm focusing; and, after passing through several pinholes and filters, it was spectrally analyzed by using a high sensitivity Si CCD camera (Synapse, Horiba) attached to a monochromator (iH320, Horiba).[52] The on-focus temperature increase (caused by the 808 nm induced plasmon excitation of GNPs) can be then estimated from the spectral shift induced in the CdSe-QDs emission (see Figure 3). Note that in our case the heating nanoparticle and the nanothermometer are separated in space as they do not constitute a single nanostructure. Therefore, the measured temperature corresponds to the averaged over the detection volume. In addition, the axial resolution of our experimental setup was estimated to be close to 25 μm. In this axial range, the averaged 488 nm "probe" and 808 nm "pump" beam waists were calculated to be 1.6 and 2.1 μm, respectively. Thus, in the detection volume, the 488 nm probe beam is, on average, more focused than the 808 nm pump one. As a consequence, the temperature determined by the 488 nm excited QDs fluorescence can be unequivocally attributed to the on-focus temperature. In each case, the emission wavelength was identified to the wavelength at which maximum intensity is emitted. The uncertainty in the determination of the emission wavelength of QDs was evaluated by performing several measurements and calculating the standard deviation of experimental data. In our experimental conditions, we have found that the uncertainty in the emission wavelength was in the order of 0.1 nm, leading to a temperature uncertainty of about 1 °C. Previous models concerning laser-induced thermal loading of static microfluidics concluded that the laser-induced temperature increase at focus, ΔT_f, can be written as[62]

$$\Delta T_f = \frac{P_{in}\alpha_{abs}}{2\pi K}\ln\left[\frac{D}{w_l}\right] = \frac{P_{in}\Phi_{abs}\alpha_{ext}}{2\pi K}\ln\left[\frac{D}{w_l}\right] \quad (1)$$

where K is the thermal conductivity of water (0.6 W/m·K), D is the chamber thickness (100 μm), P_{in} is the 808 nm laser power reaching the solution, and w_l is the 808 nm laser beam waist (0.88 μm). Thus, the on focus temperature increment normalized to the absorption coefficient ($\Delta T_f/\alpha_{ext}$) is predicted to be proportional to both the absorption efficiency and to the 808 nm laser power (P_{in}):

$$\Delta T_f/\alpha_{ext} = \frac{\Phi_{abs}}{2\pi K}\ln\left(\frac{D}{w_l}\right)P_{in} \quad (2)$$

If we define m as the slope of the $\Delta T_f/\alpha_{ext}$ vs P_{in} curve ($m = (d(\Delta T_f/\alpha_{ext})/dP_{in})$), then $\Delta T_f/\alpha_{ext} = mP_{in}$, where $m = (\Phi_{abs}/2\pi K)\ln(D/w_l)$. Thus, we can write:

$$\Phi_{abs} = m\frac{2\pi K}{\ln\left(\frac{D}{w_l}\right)} \quad (3)$$

so that the absorption efficiency of the GNPs can be obtained from the linear fit of the $\Delta T_f/\alpha_{ext}$ vs P_{in} experimental data.

RESULTS AND DISCUSSION

Figure 4 shows the laser power dependence of the $\Delta T_f/\alpha_{ext}$ ratio, as obtained for the solutions containing the five different

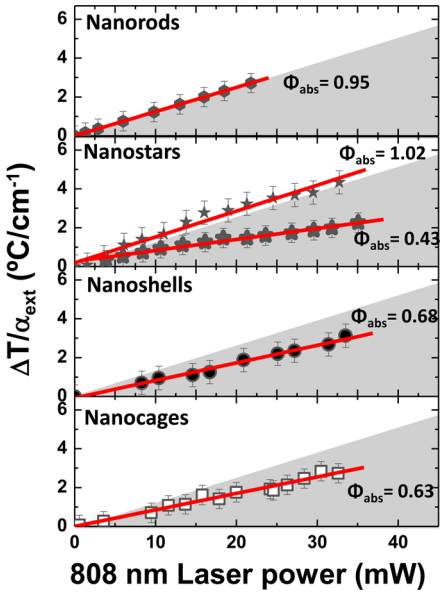

Figure 4. 808 nm laser power dependence of the on-focus temperature increase (ΔT_f), normalized by the extinction coefficient at 808 nm ($\Delta T_f/\alpha_{ext}$), as obtained for the five GNP. Dots are experimental data, and solid lines are the best linear fits. Shadowed areas indicate the conditions with physical meaning, that is, corresponding to absorption efficiencies between 0 and 1.

GNPs under study. In all cases, a linear relationship was observed, in agreement with eq 2. This suggests that the extinction coefficient of the solution at the pump wavelength (808 nm) is not modified during the heating process; that is, it is not affected by the 808 nm pump laser itself. As mentioned above, the extinction coefficient of the solution depends on the concentration of GNPs and on their extinction cross section (σ_{ext}), through the relation: $\alpha_{ext} = \sigma_{ext}[GNP]$. The local concentration of GNPs at the laser spot can, in principle, change because of the presence of optical trapping.[63,64] Previous works dealing with optical trapping of GNRs report such effects for laser intensities above 2×10^6 W/cm^2,[63] whereas in our case the maximum laser powers used were 40 mW, corresponding to a maximum laser intensity close to 0.2×10^6 W/cm^2, that is, one order of magnitude lower than the minimum intensity required for optical trapping. Thus, optical trapping is not expected to occur in our experimental conditions. Moreover, the extinction cross section of GNPs can change if their morphology is modified, that is, if reshaping takes place.[65] It should be noted that, according to previous works, reshaping of GNPs is expected to occur for temperatures above 70 °C (this number being in agreement with thermal stability experiments also carried out in our laboratory).[66−69] The local temperatures achieved during our experiments do not exceed 40 °C, that is, well below the threshold temperature for reshaping. We therefore claim that, in our experimental conditions, neither optical trapping nor laser heat induced reshaping take place. As a consequence, the extinction coefficient of the solution is not expected to vary during the

dx.doi.org/10.1021/la403435v | Langmuir XXXX, XXX, XXX−XXX

experiments, in agreement with the linear relation between $\Delta T_f/\alpha_{ext}$ and P_{in} observed in all cases. In addition, though not shown here for the sake of brevity, we also measured the 808 nm laser power dependence of the $\Delta T_f/\alpha_{ext}$ ratio for different concentrations of GNPs. No significant differences with respect to the results included in Figure 4 were found. In Figure 4, we marked (shadowed areas) the areas in the $\Delta T_f/\alpha_{ext}$ vs P_{in} plots with physical meaning, that is, those corresponding to absorption efficiency values between 0 and 1. In all cases, except the experimental data corresponding to the GNSt-l, the experimental data lie within this range. For the case of GNSt-l, some of the experimental data are slightly above this range. The difference between experimental data and the upper limit corresponding to $\Phi_{abs} = 1$ for each laser power was, in all cases, within experimental uncertainty. These facts suggest that the absorption efficiency of GNSt-l can be considered equal to unity. The absorption efficiency of each type of GNP was obtained by linear fitting of the experimental data and then applying eq 3. The results are shown in Figure 4, and the experimentally obtained absorption efficiencies are listed in Table 1. Next, the agreement between experimental values and numerical simulations is discussed.

For GNRs, the heating efficiency was found to be 95 ± 4% (Figure 4). This absorption efficiency can be compared to that previously reported for 808 nm excited GNRs of similar aspect ratios but provided by a different manufacturer (Nanopartz Inc.) and also measured by DBFT.[52] In addition, this heating efficiency is also close to that recently estimated for GNRs with SPR at 800 nm by photoacoustic imaging (85%).[47] These experimental values of Φ_{abs} are indeed in excellent agreement with theoretical simulations on the optical properties of GNRs with λ_{SPR} and aspect ratio close to 808 nm and 3, respectively.[52,70] Such calculations indicate that, for GNRs similar to those studied in this work, absorption accounts for virtually the whole optical extinction.

Figure 4 also shows the experimental results obtained for both short and long GNSts. The absorption efficiency was found to be strongly dependent on the particular morphology of the GNSts. Whereas for "long" GNSts (GNSt-l) the absorption efficiency is 102 ± 3% (virtually 100%), it drops to 43 ± 5% for the "short" GNSts (GNSt-s). This is in agreement with previous calculations performed by different research groups, which concluded that sharper tips should lead to larger absorption efficiencies.[54,71] The observed reduction in the absorption efficiency is reasonable, as for GNSt-s the plasmonic mode, mainly located at the lobes (tips), is expected to hybridize with that of the central core. This fact could account for a large scattering probability. Indeed, Jain et al. estimated that the absorption efficiency of gold nanospheres (geometry that could describe that of the central core of GNSts) decreased from 100% down to 70% when λ_{SPR} was red-shifted from 500 to 600 nm.[70] In GNSt-s, the contribution of the central core to the whole volume of a single NP is larger than for GNSt-l. Consequently, the relative contribution of core-induced scattering processes is expected to be larger for GNSt-s than for GNSt-l, therefore leading to a reduction in the absorption efficiency. The large absorption efficiency obtained for GNSt-l, together with their characteristic large surface-to-volume ratios render them promising candidates for photo-activated drug delivery therapies.

For the case of GNSs, the absorption efficiency was found to be around 68 ± 3% (see Figure 4). To check the agreement between our experimental results and theoretical predictions we recall the numerical simulations included in the work published by Jain et al., who calculated the extinction, scattering and absorption coefficients for GNSs with a silica (core) radius of 50 nm and a gold shell thickness of 10 nm, similar dimensions to those of our GNSs.[70] For those dimensions, the calculated λ_{SPR} was 890 nm (very close to the λ_{SPR} estimated from the extinction spectrum included in Figure 2: 870 nm) and the calculated absorption efficiency was close to 64%, which is in excellent agreement with our experimental data. According to our experimental data, the absorption/heating efficiency of GNSs is 0.7 times the heating efficiency of GNRs. This is in good agreement with the comparative studies performed by Hessel et al. who experimentally found that the photothermal efficiency of a solution of GNSs was 0.6 times that of a GNR solution (both excited at 800 nm).[72]

Finally, Figure 4 also includes the results obtained for the GNCs. The obtained absorption efficiency, 63 ± 2%, is similar to those obtained for GNSs and GNSts-s. A review of previous publications concerning the absorption and scattering properties of GNCs shows that a wide variety can be found in the values of absorption efficiencies, ranging from 40% up to 100%. Such a large variation is due to the strong influence that both, the wall thickness and edge dimensions have on the optical properties of GNCs. When previously published simulations of both scattering and absorption cross sections of GNCs are reviewed it is found that, for a fixed wall thickness around 5 nm, the absorption efficiency decreases with edge length.[55,73,74] Based on these numerical calculations, for our GNCs (47 nm edge length and 4 nm wall thickness) an absorption efficiency close to 70% was expected. Indeed, this can be compared to that we have here obtained experimentally (63%), recalling what possible differences could arise from the deviation of the GNC geometry from that of a perfect cube (assumed in numerical simulations).[75] It should be mentioned that the absorption efficiency found from GNCs is the lowest one among the geometries analyzed in this work. This also agrees with the calculations performed by Hu et al., who compared the absorption efficiency of GNRs, GNSs and GNCs (all of them with λ_{SPR} at 800 nm), concluding that GNCs showed the lowest absorption efficiency.[74] Thus, again, our experimental data agree well with theoretical simulations.

Once Φ_{abs} is known, it is possible to determine both the scattering and absorption cross sections from the extinction coefficients determined by optical transmission experiments: $\sigma_{abs} = \sigma_{ext}\cdot\Phi_{abs}$ and $\sigma_{scat} = \sigma_{ext}\cdot(1\text{-}\Phi_{abs})$. Table 1 includes the obtained extinction, absorption and scattering cross sections per GNP. The largest absorption cross sections correspond to GNCs and GNSs, both showing absorption cross sections in the order of 10^{-10} cm^2 per nanoparticle. For the purpose of real "in vivo" photothermal treatments, it would be desirable to keep at a minimum the total amount of gold incorporated into the biosystem. This would minimize the possible adverse effects caused by high metal mass loadings. In this respect, GNPs with large absorption cross section per nanoparticle and reduced nanoparticle mass would be desirable. Thus we also listed in Table 1 the gold mass per nanoparticle ([Au]) corresponding to the five different geometries. Based on these masses we estimated the single particle absorption cross section per unit mass (σ_{abs}/[Au]): Results are also listed in Table 1. The largest values, in the range of 10^6 cm^2/g, were obtained for GNRs and GNCs, being slightly larger for GNRs. This fact, together with the excellent uptake rate of GNRs by tumors suggests that these nanoparticles are very promising for efficient and low

dx.doi.org/10.1021/la403435v | Langmuir XXXX, XXX, XXX−XXX

invasive photothermal treatments.[47] Nevertheless, at this point it should be mentioned that other GNPs with reduced absorption efficiencies could be also of great utility in, for instance, photothermal treatments requiring real time GNP optical tracking. For this purpose, GNPs with both remarkable scattering and absorption cross sections would be desirable. Inspection of the values listed in Table 1 reveals that GNCs simultaneously show large absorption and scattering cross sections (both in the order of 10^{-10} cm^2) so they constitute good candidates for efficient photothermal therapies with real time tracking under single beam illumination.

■ CONCLUSIONS

In summary, quantum dot fluorescence nanothermometry in combination with double beam confocal microscopy was used to determine the heating/absorbing efficiency of gold nanoparticles of different geometries all of them with surface plasmon resonances close to 808 nm, that is, within the first transparency window for cells and tissue. It has been observed that the heating efficiency of gold nanoparticles strongly depends on the particular geometry of the nanoparticles. Gold nanorods and long-edge gold nanostars were found to be the geometries leading to absorption efficiencies close to unity. Furthermore, GNRs were found to provide the largest absorption cross section per unit mass, rendering them the most promising candidates for efficient photothermal therapies. Absorption efficiencies experimentally determined for all the geometries were compared to those previously predicted by numerical simulations, with good agreement. The results here reported open new opportunities for further optimization of photothermal therapies based on gold nanoparticles, by an adequate preselection of their exact geometry and size.

■ AUTHOR INFORMATION

Notes

The authors declare no competing financial interest.

■ ACKNOWLEDGMENTS

L.M.L.-M. acknowledges financial support from the European Research Council (ERC Advanced Grant #267867 Plasmaquo). This work was supported by the Universidad Autónoma de Madrid and Comunidad Autónoma de Madrid (Project S2009/MAT- 1756), by the Spanish Ministerio de Educacion y Ciencia (MAT2010-16161). L.M.M. thanks the Spanish Ministerio de Economia y Competitividad (MINECO) for a FPI grant. P.H.-G. thanks Fundación Doctor Manuel Morales and Ministerio de Economia y Competitividad (subprograma Juan de la Cierva) for financial support.

■ REFERENCES

(1) Wust, P.; Hildebrandt, B.; Sreenivasa, G.; Rau, B.; Gellermann, J.; Riess, H.; Felix, R.; Schlag, P. M. Hyperthermia in Combined Treatment of Cancer. *Lancet Oncol.* **2002**, *3* (8), 487−497.

(2) O'Neal, D. P.; Hirsch, L. R.; Halas, N. J.; Payne, J. D.; West, J. L. Photo-Thermal Tumor Ablation in Mice Using near Infrared-Absorbing Nanoparticles. *Cancer Lett.* **2004**, *209* (2), 171−176.

(3) Dinarvand, R.; Khodaverdi, E.; Atyabi, F.; Erfan, M. Thermoresponsive Drug Delivery Using Liquid Crystal-Embedded Cellulose Nitrate Membranes. *Drug Delivery* **2006**, *13* (5), 345−350.

(4) Johannsen, M.; Gneveckow, U.; Eckelt, L.; Feussner, A.; Waldöfner, N.; Scholz, R.; Deger, S.; Wust, P.; Loening, S. A.; Jordan, A. Clinical Hyperthermia of Prostate Cancer Using Magnetic Nanoparticles: Presentation of a New Interstitial Technique. *Int. J. Hyperthermia* **2005**, *21* (7), 637−647.

(5) Huang, X.; Jain, P. K.; El-Sayed, I. H.; El-Sayed, M. A. Determination of the Minimum Temperature Required for Selective Photothermal Destruction of Cancer Cells with the Use of Immunotargeted Gold Nanoparticles. *Photochem. Photobiol.* **2006**, *82* (2), 412−417.

(6) Torti, S. V.; Byrne, F.; Whelan, O.; Levi, N.; Ucer, B.; Schmid, M.; Torti, F. M.; Akman, S.; Liu, J.; Ajayan, P. M.; Nalamasu, O.; Carroll, D. L. Thermal Ablation Therapeutics Based on CN(x) Multi-Walled Nanotubes. *Int. J. Nanomed.* **2007**, *2* (4), 707−714.

(7) Vetrone, F.; Naccache, R.; Zamarron, A.; Juarranz de la Fuente, A.; Sanz-Rodriguez, F.; Martinez Maestro, L.; Martin Rodriguez, E.; Jaque, D.; Garcia Sole, J.; Capobianco, J. A. Temperature sensing using fluorescent nanothermometers. *ACS Nano* **2010**, *4* (6), 3254−8.

(8) Jaque, D.; Vetrone, F. Luminescence Nanothermometry. *Nanoscale* **2012**, *4* (15), 4301−4326.

(9) Gota, C.; Okabe, K.; Funatsu, T.; Harada, Y.; Uchiyama, S. Hydrophilic Fluorescent Nanogel Thermometer for Intracellular Thermometry. *J. Am. Chem. Soc.* **2009**, *131* (8), 2766−2767.

(10) Uchiyama, S.; Matsumura, Y.; de Silva, A. P.; Iwai, K. Fluorescent Molecular Thermometers Based on Polymers Showing Temperature-Induced Phase Transitions and Labeled with Polarity-Responsive Benzofurazans. *Anal. Chem.* **2003**, *75* (21), 5926−5935.

(11) Okabe, K.; Inada, N.; Gota, C.; Harada, Y.; Funatsu, T.; Uchiyama, S. Intracellular Temperature Mapping with a Fluorescent Polymeric Thermometer and Fluorescence Lifetime Imaging Microscopy. *Nat. Commun.* **2012**, *3*, 705.

(12) Rocha, U.; Jacinto da Silva, C.; Ferreira Silva, W.; Guedes, I.; Benayas, A.; Martínez Maestro, L.; Acosta Elias, M.; Bovero, E.; van Veggel, F. C. J. M.; García Solé, J. A.; Jaque, D. Subtissue Thermal Sensing Based on Neodymium-Doped LaF3 Nanoparticles. *ACS Nano* **2013**, *7* (2), 1188−1199.

(13) Yang, J. M.; Yang, H.; Lin, L. Quantum Dot Nanothermometers Reveal Heterogeneous Local Thermogenesis in Living Cells. *ACS Nano* **2011**, *5* (6), 5067−5071.

(14) Peng, H.-S.; Huang, S.-H.; Wolfbeis, O. Ratiometric Fluorescent Nanoparticles for Sensing Temperature. *J. Nanopart. Res.* **2010**, *12* (8), 2729−2733.

(15) Carlson, M. T.; Green, A. J.; Richardson, H. H. Superheating Water by CW Excitation of Gold Nanodots. *Nano Lett.* **2012**, *12*, 1534−1537.

(16) Lee, J.; Govorov, A. O.; Kotov, N. A. Nanoparticle Assemblies with Molecular Springs: A Nanoscale Thermometer. *Angew. Chem., Int. Ed.* **2005**, *44* (45), 7439−7442.

(17) Setoura, K.; Werner, D.; Hashimoto, S. Optical Scattering Spectral Thermometry and Refractometry of a Single Gold Nanoparticle under CW Laser Excitation. *J. Phys. Chem. C* **2012**, *116* (29), 15458−15466.

(18) Debasu, M. L.; Ananias, D.; Pastoriza-Santos, I.; Liz-Marzán, L. M.; Rocha, J.; Carlos, L. D. Nanothermometry: All-In-One Optical Heater-Thermometer Nanoplatform Operative From 300 to 2000 K Based on Er3+ Emission and Blackbody Radiation. *Adv. Mater.* **2013**, *25* (35), 4817−4817.

(19) Carlson, M. T.; Green, A. J.; Khan, A.; Richardson, H. H. Optical Measurement of Thermal Conductivity and Absorption Cross-Section of Gold Nanowires. *J. Phys. Chem. C* **2012**, *116* (15), 8798−8803.

(20) Brites, C. D. S.; Lima, P. P.; Silva, N. J. O.; Millan, A.; Amaral, V. S.; Palacio, F.; Carlos, L. D. Thermometry at the Nanoscale. *Nanoscale* **2012**, *4* (16), 4799−4829.

(21) Wang, X.-d.; Wolfbeis, O. S.; Meier, R. J. Luminescent Probes and Sensors for Temperature. *Chem. Soc. Rev.* **2013**, *42* (19), 7834−7869.

(22) Kam, N. W. S.; O'Connell, M.; Wisdom, J. A.; Dai, H. J. Carbon Nanotubes As Multifunctional Biological Transporters and near-Infrared Agents for Selective Cancer Cell Destruction. *Proc. Natl. Acad. Sci. U.S.A.* **2005**, *102* (33), 11600−11605.

(23) Malam, Y.; Loizidou, M.; Seifalian, A. M. Liposomes and Nanoparticles: Nanosized Vehicles for Drug Delivery in Cancer. *Trends Pharmacol. Sci.* **2009**, *30* (11), 592−599.

(24) Maestro, L. M.; Haro-González, P.; Iglesias-de la Cruz, M. C.; Sanz-Rodríguez, F.; Juarranz, A.; Solé, J. G.; Jaque, D. Fluorescent Nanothermometers Provide Controlled Plasmonic-Mediated Intracellular Hyperthermia. *Nanomedicine* **2013**, *8*, 379−388.
(25) Zhou, F. F.; Xing, D.; Ou, Z. M.; Wu, B. Y.; Resasco, D. E.; Chen, W. R. Cancer Photothermal Therapy in the near-Infrared Region by Using Single-Walled Carbon Nanotubes. *J. Biomed. Opt.* **2009**, *14*, 021009.
(26) Hergt, R.; Hiergeist, R.; Hilger, I.; Kaiser, W. A.; Lapatnikov, Y.; Margel, S.; Richter, U. Maghemite Nanoparticles with Very High AC-Losses for Application in RF-Magnetic Hyperthermia. *J. Magn. Magn. Mater.* **2004**, *270* (3), 345−357.
(27) Gilchrist, R. K.; Medal, R.; Shorey, W. D.; Hanselman, R. C.; Parrott, J. C. Selective Inductive Heating of Lymph Nodes. *Ann. Surg.* **1957**, *146* (4), 596−606.
(28) Jordan, A.; Scholz, R.; Maier-Hauff, K.; Johannsen, M.; Wust, P.; Nadobny, J.; Schirra, H.; Schmidt, H.; Deger, S.; Loening, S.; Lanksch, W.; Felix, R. Presentation of a New Magnetic Field Therapy System for the Treatment of Human Solid Tumors with Magnetic Fluid Hyperthermia. *J. Magn. Magn. Mater.* **2001**, *225* (1−2), 118−126.
(29) Jordan, A.; Scholz, R.; Wust, P.; Fähling, H.; Roland, F. Magnetic Fluid Hyperthermia (MFH): Cancer Treatment with AC Magnetic Field Induced Excitation of Biocompatible Superparamagnetic Nanoparticles. *J. Magn. Magn. Mater.* **1999**, *201* (1−3), 413−419.
(30) Prokop, A. *Intracellular Delivery: Fundamentals and Applications*; Springer: Dordrecht, Heidelberg, London, New York, 2011; Vol. *5*.
(31) Smith, A. M.; Mancini, M. C.; Nie, S. Bioimaging: Second Window for in Vivo Imaging. *Nat. Nanotechnol.* **2009**, *4* (11), 710−711.
(32) König, K. Multiphoton Microscopy in Life Sciences. *J. Microsc.* **2000**, *200* (2), 83−104.
(33) Maestro, L. M.; Haro-Gonzalez, P.; del Rosal, B.; Ramiro, J.; Caamano, A. J.; Carrasco, E.; Juarranz, A.; Sanz-Rodriguez, F.; Sole, J. G.; Jaque, D. Heating Efficiency of Multi-Walled Carbon Nanotubes in the First and Second Biological Windows. *Nanoscale* **2013**, *5*, 7882−7889.
(34) Anderson, R. R.; Parrish, J. A. The optics of human skin. *J. Invest. Dermatol.* **1981**, *77* (1), 13−19.
(35) Pissuwan, D.; Valenzuela, S. M.; Cortie, M. B. Therapeutic Possibilities of Plasmonically Heated Gold Nanoparticles. *Trends Biotechnol.* **2006**, *24* (2), 62−67.
(36) Tong, L.; He, W.; Zhang, Y.; Zheng, W.; Cheng, J.-X. Visualizing Systemic Clearance and Cellular Level Biodistribution of Gold Nanorods by Intrinsic Two-Photon Luminescence. *Langmuir* **2009**, *25* (21), 12454−12459.
(37) He, W.; Henne, W.; Wei, Q.; Zhao, Y.; Doorneweerd, D.; Cheng, J.-X.; Low, P.; Wei, A. Two-Photon Luminescence Imaging of Bacillus Spores Using Peptide-Functionalized Gold Nanorods. *Nano Res.* **2008**, *1* (6), 450−456.
(38) Gilchrist, R. K.; Medal, R.; Shorey, W. D.; Hanselman, R. C.; Parrott, J. C.; Taylor, C. B. Selective Inductive Heating of Lymph Nodes. *Ann. Surg.* **1957**, *146* (4), 596−606.
(39) Kang, H.; Jia, B. H.; Li, J. L.; Morrish, D.; Gu, M. Enhanced Photothermal Therapy Assisted with Gold Nanorods Using a Radially Polarized Beam. *Appl. Phys. Lett.* **2010**, *96*, 063702.
(40) Baffou, G.; Quidant, R.; Girard, C. Heat Generation in Plasmonic Nanostructures: Influence of Morphology. *Appl. Phys. Lett.* **2009**, *94* (15), 153109.
(41) Bickford, L.; Sun, J.; Fu, K.; Lewinski, N.; Nammalvar, V.; Chang, J.; Drezek, R. Enhanced Multi-Spectral Imaging of Live Breast Cancer Cells Using Immunotargeted Gold Nanoshells and Two-Photon Excitation Microscopy. *Nanotechnology* **2008**, *19* (31), 315102.
(42) Pérez-Juste, J.; Pastoriza-Santos, I.; Liz-Marzán, L. M.; Mulvaney, P. Gold Nanorods: Synthesis, Characterization and Applications. *Coord. Chem. Rev.* **2005**, *249* (17−18), 1870−1901.
(43) Terentyuk, G. S.; Maslyakova, G. N.; Suleymanova, L. V.; Khlebtsov, N. G.; Khlebtsov, B. N. Laser-Induced Tissue Hyperthermia Mediated by Gold Nanoparticles: Toward Cancer Phototherapy. *J. Biomed. Opt.* **2009**, *14* (2), 021016.
(44) Kang, H.; Jia, B.; Li, J.; Morrish, D.; Gu, M. Enhanced Photothermal Therapy Assisted with Gold Nanorods Using a Radially Polarized Beam. *Appl. Phys. Lett.* **2010**, *96* (6), 063702.
(45) Skrabalak, S. E.; Chen, J.; Au, L.; Lu, X.; Li, X. Gold Nanocages for Biomedical Applications. *Adv. Mater.* **2007**, *19* (20), 3177−3184.
(46) Yuan, H.; Khoury, C. G.; Wilson, C. M.; Grant, G. A.; Bennett, A. J. In Vivo Particle Tracking and Photothermal Ablation Using Plasmon-Resonant Gold Nanostars. *Nanomedicine* **2012**, *8* (8), 1355−63.
(47) Wang, Y.; Black, K. C.; Luehmann, H.; Li, W.; Zhang, Y.; Cai, X.; Wan, D.; Liu, S. Y.; Li, M.; Kim, P.; Li, Z. Y.; Wang, L. V.; Liu, Y.; Xia, Y. Comparison Study of Gold Nanohexapods, Nanorods, And Nanocages for Photothermal Cancer Treatment. *ACS Nano* **2013**, *7* (3), 2068−2077.
(48) Huang, X. H.; El-Sayed, I. H.; Qian, W.; El-Sayed, M. A. Cancer Cell Imaging and Photothermal Therapy in the near-Infrared Region by Using Gold Nanorods. *J. Am. Chem. Soc.* **2006**, *128* (6), 2115−2120.
(49) Maestro, L. M.; Rodriguez, E. M.; Vetrone, F.; Naccache, R.; Ramirez, H. L.; Jaque, D.; Capobianco, J. A.; Sole, J. G. Nanoparticles for Highly Efficient Multiphoton Fluorescence Bioimaging. *Opt. Express* **2010**, *18* (23), 23544−23553.
(50) Wang, H.; Huff, T. B.; Zweifel, D. A.; He, W.; Low, P. S.; Wei, A.; Cheng, J.-X. *In Vitro* and *in Vivo* Two-Photon Luminescence Imaging of Single Gold Nanorods. *Proc. Natl. Acad. Sci. U.S.A.* **2005**, *102*, 15752−15756.
(51) Jain, P. K.; Lee, K. S.; El-Sayed, I. H.; El-Sayed, M. A. Calculated Absorption and Scattering Properties of Gold Nanoparticles of Different Size, Shape, and Composition: Applications in Biological Imaging and Biomedicine. *J. Phys. Chem. B* **2006**, *110* (14), 7238−7248.
(52) Maestro, L. M.; Haro-Gonzalez, P.; Coello, J. G.; Jaque, D. Absorption Efficiency of Gold Nanorods Determined by Quantum Dot Fluorescence Thermometry. *Appl. Phys. Lett.* **2012**, *100* (20), 201110.
(53) Link, S.; Mohamed, M. B.; El-Sayed, M. A. Simulation of the Optical Absorption Spectra of Gold Nanorods as a Function of Their Aspect Ratio and the Effect of the Medium Dielectric Constant. *J. Phys. Chem. B* **1999**, *103* (16), 3073−3077.
(54) Rodríguez-Oliveros, R.; Sánchez-Gil, J. A. Gold Nanostars as Thermoplasmonic Nanoparticles for Optical Heating. *Opt. Express* **2012**, *20* (1), 621−626.
(55) Cho, E. C.; Kim, C.; Zhou, F.; Cobley, C. M.; Song, K. H.; Chen, J.; Li, Z. Y.; Wang, L. V.; Xia, Y. Measuring the Optical Absorption Cross Sections of Au-Ag Nanocages and Au Nanorods by Photoacoustic Imaging. *J. Phys. Chem. C* **2009**, *113* (21), 9023−9028.
(56) Yuan, H.; Khoury, C. G.; Hwang, H.; Wilson, C. M.; Grant, G. A.; Vo-Dinh, T. Gold Nanostars: Surfactant-Free Synthesis, 3D Modelling, and Two-Photon Photoluminescence Imaging. *Nanotechnology* **2012**, *23* (7), 075102.
(57) Senthil Kumar, P.; Pastoriza-Santos, I.; Rodriguez-Gonzalez, B.; Javier Garcia de Abajo, F.; Liz-Marzan, L. M. High-Yield Synthesis and Optical Response of Gold Nanostars. *Nanotechnology* **2008**, *19* (1), 015606.
(58) Zhang, Q.; Li, W.; Wen, L. P.; Chen, J.; Xia, Y. Facile Synthesis of Ag Nanocubes of 30 to 70 nm in Edge Length With CF(3)COOAg as a Precursor. *Chemistry* **2010**, *16* (33), 10234−9.
(59) Sun, Y.; Xia, Y. Mechanistic Study on the Replacement Reaction between Silver Nanostructures and Chloroauric Acid in Aqueous Medium. *J. Am. Chem. Soc.* **2004**, *126* (12), 3892−901.
(60) Albers, A. E.; Chan, E. M.; McBride, P. M.; Ajo-Franklin, C. M.; Cohen, B. E.; Helms, B. A. Dual-Emitting Quantum Dot/Quantum Rod-Based Nanothermometers with Enhanced Response and Sensitivity in Live Cells. *J. Am. Chem. Soc.* **2012**, *134* (23), 9565−9568.
(61) Maestro, L. M.; Rodriguez, E. M.; Rodriguez, F. S.; la Cruz, M. C. I.; Juarranz, A.; Naccache, R.; Vetrone, F.; Jaque, D.; Capobianco, J. A.; Sole, J. G. CdSe Quantum Dots for Two-Photon Fluorescence Thermal Imaging. *Nano Lett.* **2010**, *10* (12), 5109−5115.

(62) Mao, H.; Ricardo Arias-Gonzalez, J.; Smith, S. B.; Tinoco, I.; Bustamante, C. Temperature Control Methods in a Laser Tweezers System. *Biophys. J.* **2005**, *89* (2), 1308−1316.
(63) Selhuber-Unkel, C.; Zins, I.; Schubert, O.; Sönnichsen, C.; Oddershede, L. B. Quantitative Optical Trapping of Single Gold Nanorods. *Nano Lett.* **2008**, *8* (9), 2998−3003.
(64) Zhang, Y.; Gu, C.; Schwartzberg, A. M.; Chen, S.; Zhang, J. Z. Optical Trapping and Light-Induced Agglomeration of Gold Nanoparticle Aggregates. *Phys. Rev. B* **2006**, *73* (16), 165405.
(65) Lukianova-Hleb, E. Y.; Anderson, L. J. E.; Lee, S.; Hafner, J. H.; Lapotko, D. O. Hot Plasmonic Interactions: A New Look at the Photothermal Efficacy of Gold Nanoparticles. *Phys. Chem. Chem. Phys.* **2010**, *12* (38), 12237−12244.
(66) Zijlstra, P.; Chon, J. W.; Gu, M. Five-Dimensional Optical Recording Mediated by Surface Plasmons in Gold Nanorods. *Nature* **2009**, *459* (7245), 410−3.
(67) Hironobu, T.; Takuro, N.; Ayuko, N.; Yasuro, N.; Sunao, Y. Photothermal Reshaping of Gold Nanorods Prevents Further Cell Death. *Nanotechnology* **2006**, *17* (17), 4431.
(68) Mohamed, M. B.; Ismail, K. Z.; Link, S.; El-Sayed, M. A. Thermal Reshaping of Gold Nanorods in Micelles. *J. Phys. Chem. B* **1998**, *102* (47), 9370−9374.
(69) Carbo-Argibay, E.; Rodriguez-Gonzalez, B.; Pacifico, J.; Pastoriza-Santos, I.; Perez-Juste, J.; Liz-Marzan, L. M. Chemical Sharpening of Gold Nanorods: The Rod-to-Octahedron Transition. *Angew. Chem., Int. Ed.* **2007**, *46* (47), 8983−9897.
(70) Jain, P. K.; Lee, K. S.; El-Sayed, I. H.; El-Sayed, M. A. Calculated Absorption and Scattering Properties of Gold Nanoparticles of Different Size, Shape, and Composition: Applications in Biological Imaging and Biomedicine. *J. Phys. Chem. B* **2006**, *110* (14), 7238−7248.
(71) Yuan, H.; Khoury, C. G.; Wilson, C. M.; Grant, G. A.; Bennett, A. J.; Vo-Dinh, T. In Vivo Particle Tracking and Photothermal Ablation Using Plasmon-Resonant Gold Nanostars. *Nanomedicine* **2012**, *8* (8), 1355−1363.
(72) Hessel, C. M.; Pattani, V. P.; Rasch, M.; Panthani, M. G.; Koo, B. Copper Selenide Nanocrystals for Photothermal Therapy. *Nano Lett.* **2011**, *11* (6), 2560−2566.
(73) Chen, J.; Wiley, B.; Li, Z. Y.; Campbell, D.; Saeki, F. Gold Nanocages: Engineering Their Structure for Biomedical Applications. *Adv. Mater.* **2005**, *17* (18), 2255−2261.
(74) Hu, M.; Chen, J.; Li, Z.-Y.; Au, L.; Hartland, G. V.; Li, X.; Marquez, M.; Xia, Y. Gold Nanostructures: Engineering Their Plasmonic Properties for Biomedical Applications. *Chem. Soc. Rev.* **2006**, *35* (11), 1084−1094.
(75) Chen, J.; Yang, M.; Zhang, Q.; Cho, E. C.; Cobley, C. M.; Kim, C.; Glaus, C.; Wang, L. V.; Welch, M. J.; Xia, Y. Gold Nanocages: A Novel Class of Multifunctional Nanomaterials for Theranostic Applications. *Adv. Funct. Mater.* **2010**, *20* (21), 3684−3694.